- Stress tensor in Granular system
- Spintronics: Fundamentals ans applications (Zutic, Fabian, and Sarma, Rev. Mod. Phys. **76**, 323 2004)

Dec. 8

- Optical properties of III-Mn-V ferromagnetic semiconductors (Burch, Awschalom, and Basov, JMMM **320**, 3207 (2008))
- Photonic crystal (Phys. Rep. **444**, 101 (2007))
- 0 D – Practical applications of fullerene
- 1 D – Recent progress of carbon nanotube composites as a space elevator

Jan. 5

- 2 D – Graphene electronics : advantage and disadvantage
- 3 D – Quantum computation using Diamond nano-crystals

6 Bulk Nanostructured Materials

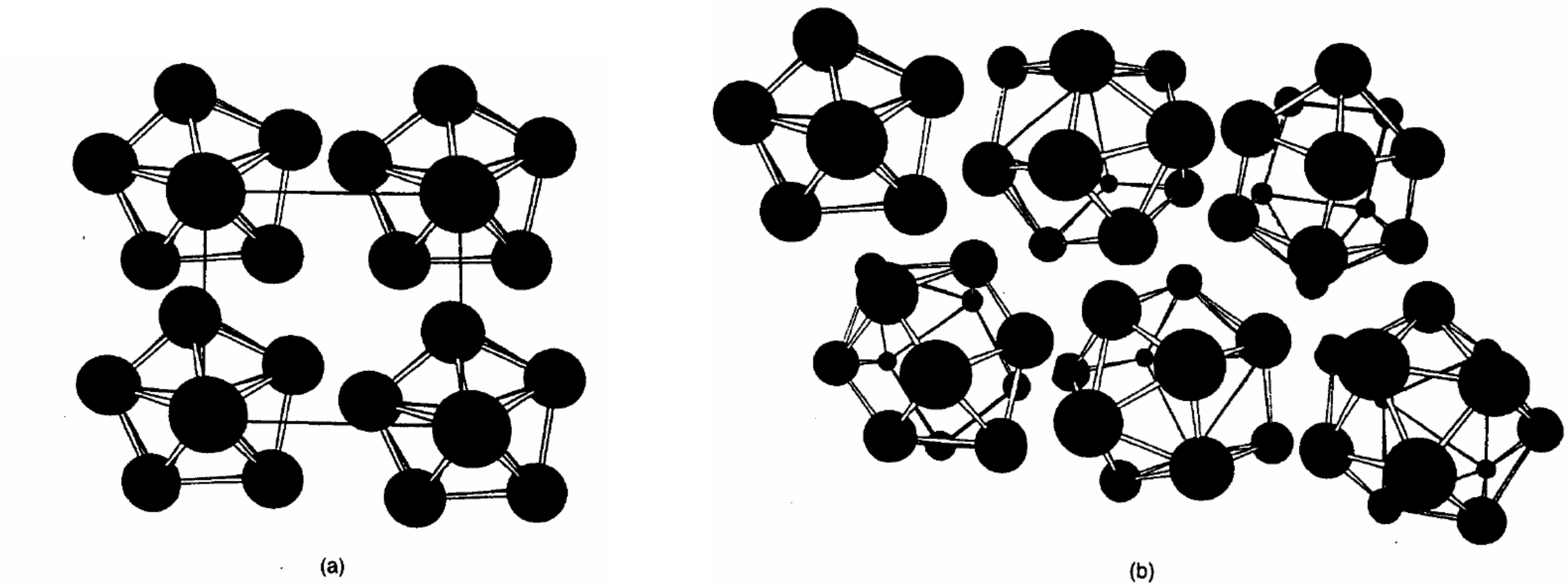

Figure 6.1. (a) Illustration of a hypothetical two-dimensional square lattice of Al_{12} particles, and (b) illustration of a two-dimensional bulk solid of Al_{12} where the nanoparticles have no ordered arrangement with respect to each other.

The Five Convex Regular Polyhedra (Platonic solids)				
Tetrahedron	Hexahedron or Cube	Octahedron	Dodecahedron	Icosahedron
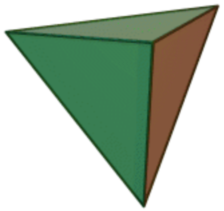	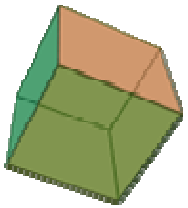	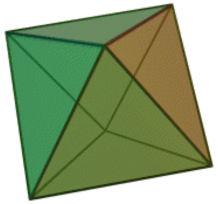	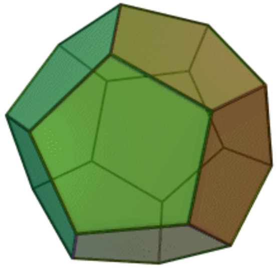	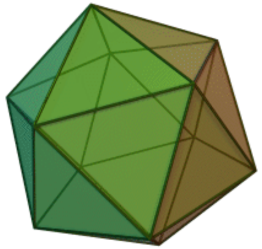

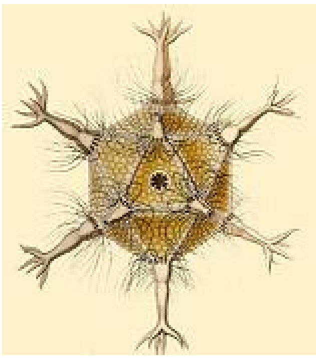

Circogonia icosahedra, a species of Radiolaria (放射蟲), shaped like a regular icosahedron.

http://en.wikipedia.org/wiki/Platonic_solid

Fabrication or synthesis

For industry, for research

- Compaction and consolidation
- Chill block melt spinning
  - Fig. 6.4
- Gas atomization
  - Fig. 6.5

- MBE
- MOCVD
- Sputter deposition
- Laser ablation
- Self assembly

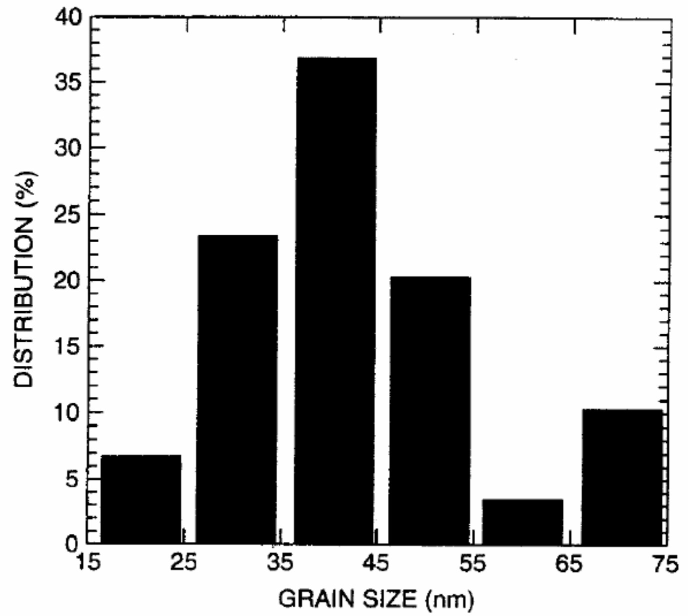

Figure 6.2. Distribution of sizes of Fe–Cu nanoparticles made by hot compaction methods described in the text. [Adapted from L. He and E. Ma, *J. Mater. Res.* **15**, 904 (2000).]

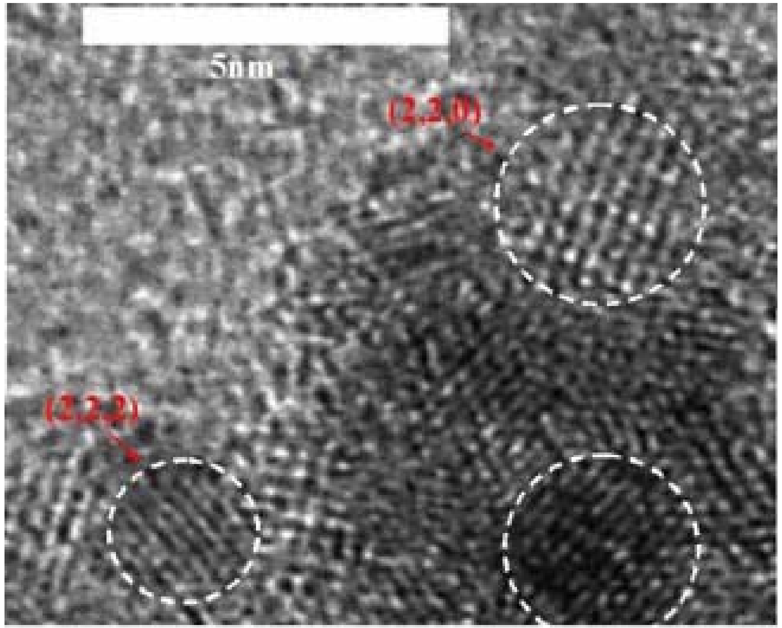

HRTEM image of 3.8 nm $CePt_2$ reveals several well-crystallized particles in which (220) and (222) planes are indicated.
Dr. Y. Y. Chen

• Mechanical properties

Tension on materials causes elongation and fractures, stess builds up on the cracks and breaks bonds. Edge and screw dislocations cause weak bonds. Grain boundary stops crack propagation.

Brittle-to ductile transition

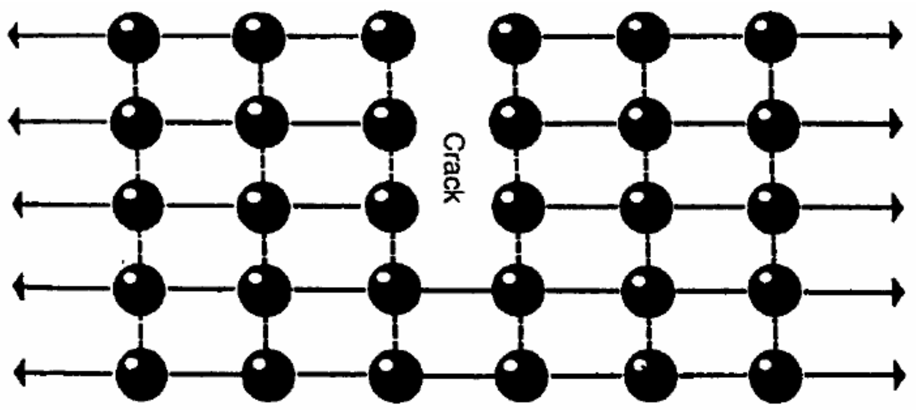

Figure 6.6. A crack in a two-dimensional rectangular lattice.

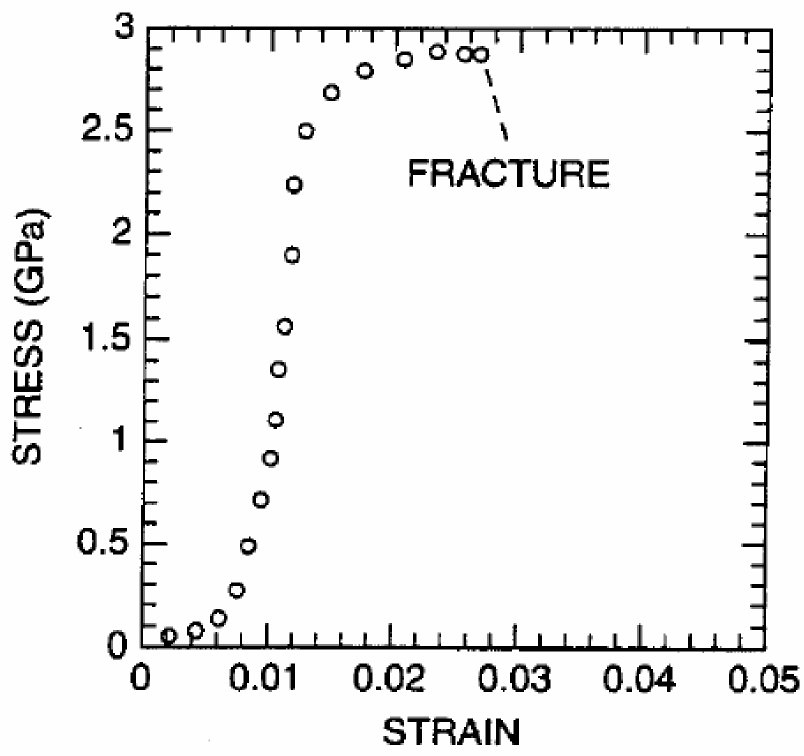

Figure 6.3. Stress–strain curve for bulk compacted nanostructured Fe–Cu material, showing fracture at a stress of 2.8 GPa. [Adapted from L. He and E. Ma, *J. Mater. Res.* **15**, 904 (2000).]

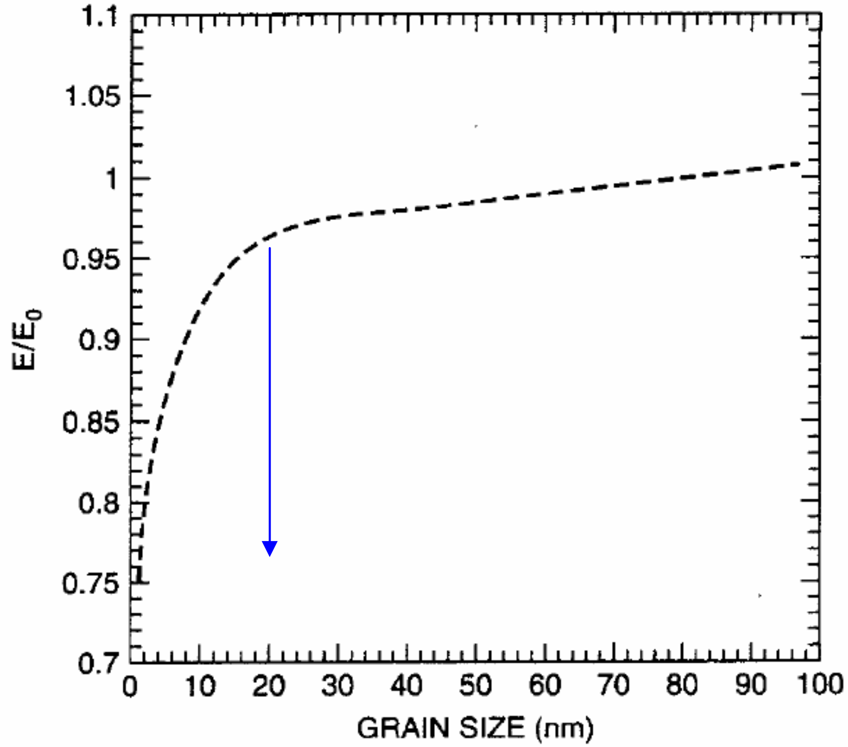

Figure 6.8. Plot of the ratio of Young's modulus E in nanograin iron to its value E_0 in conventional granular iron as a function of grain size.

Stress $S = W / A$ weight per unit cross-section

Strain $e = \Delta L / L$

$S = E e$ Hook's law

$E = L W / A \Delta L$ Young's modulus

materials which have smaller E are more elastic

Hall-Petch equation

$\sigma_y = \sigma_0 + k d^{-1/2}$

σ_0 frictional stress opposing dislocation

Fig. 6.9 This works from bulk materials down to d ~ 1μm

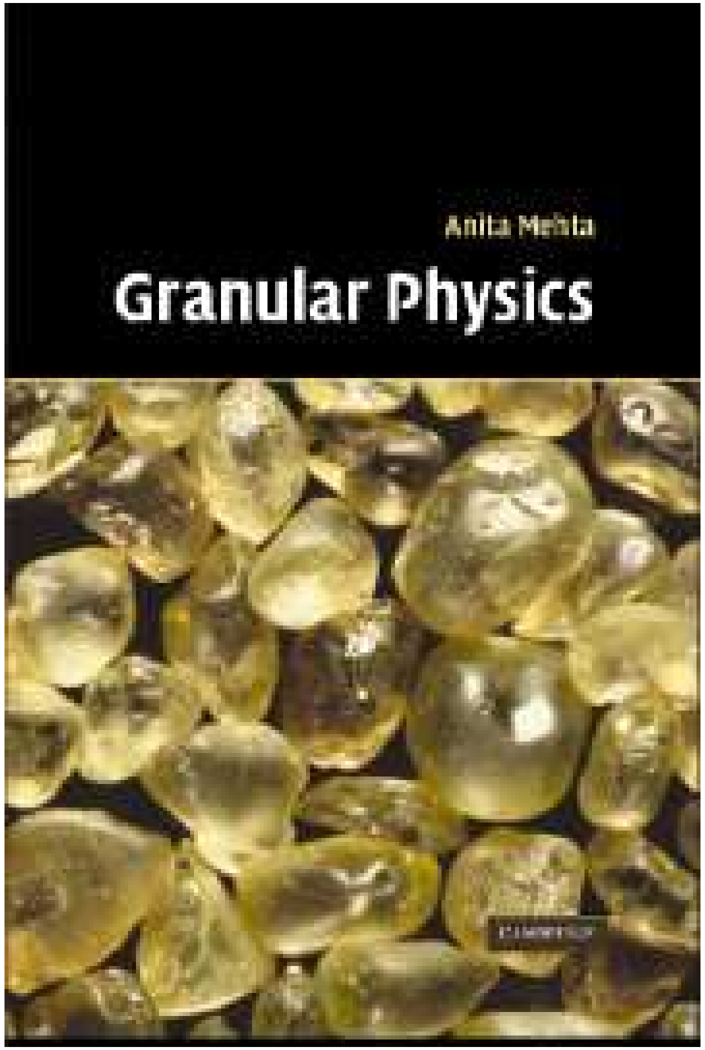

- 13 The thermodynamics of granular materials
  Sir Sam Edwards and Raphael Blumenfeld
- 13.1 Introduction
- 13.2 Statistical mechanics
- 13.3 Volume functions and forces in granular systems
- 13.4 The stress field
- 13.5 Force distribution
- 14 Static properties of granular materials
  Philippe Claudin
- 14.1 Statics at the grain scale
- 14.2 Large-scale properties
- 14.3 Conclusion

• Multilayers

Mismatch between different layers at the interfaces enhances hardness.

Hardness can be measured by a Nano-identer.

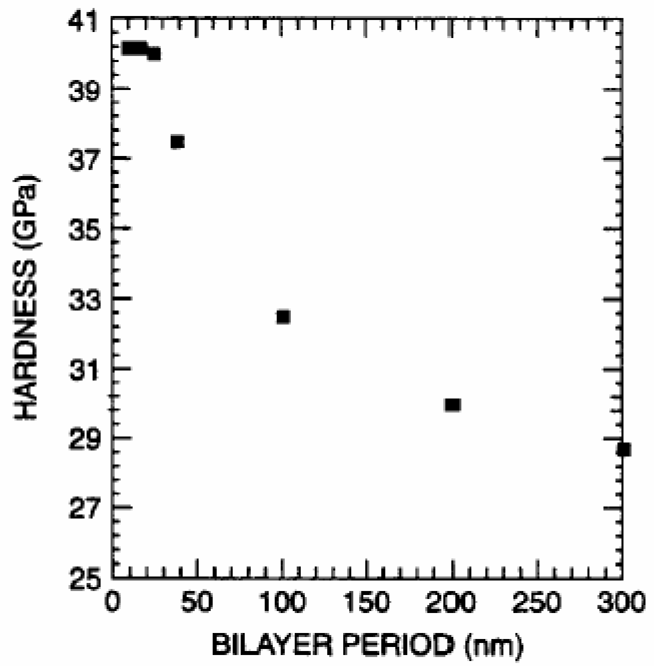

Figure 6.11. Plot of the hardness of TiN/NbN multilayer materials as a function of the thickness of the layers. (Adapted from B. M. Clemens, MRS Bulletin, Feb. 1999, p. 20.)

- Electrical properties

Au nano-particles electrically connected by long thiol molecules.

$$G = G_0 \exp (- E / k_B T)$$

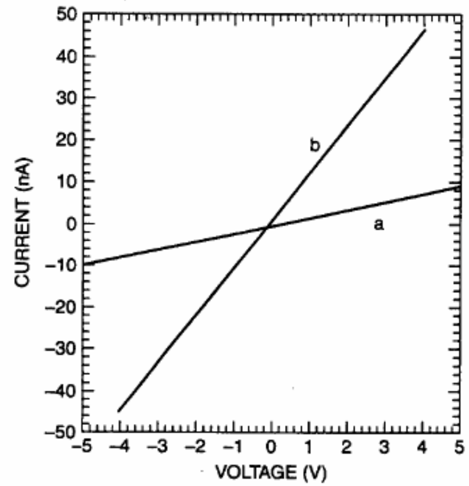

Figure 6.13. Room-temperature current–voltage relationship for a two-dimensional cluster without linkage (line a) and with the particles linked by a $(CN)_2C_{18}H_{12}$ molecule (line b). ted from D. James et al., *Superlatt. Microstruct.* **18**, 275 (1995).]

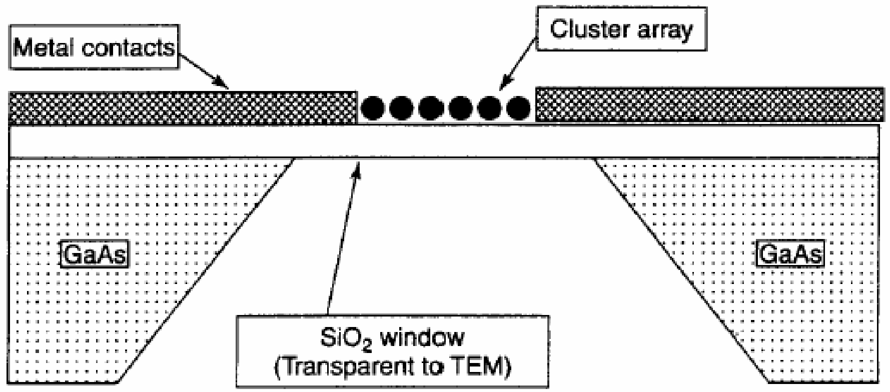

Figure 6.12. Cross-sectional view of a lithographically fabricated device to measure the electrical conductivity in a two-dimensional array of gold nanoparticles linked by molecules. (With permission from R. P Andres et al., in *Handbook of Nanostructured Materials and Nanotechnology*, H. S. Nalwa, ed., Academic Press, San Diego, 2000, Vol. 3, Chapter 4, p. 217.

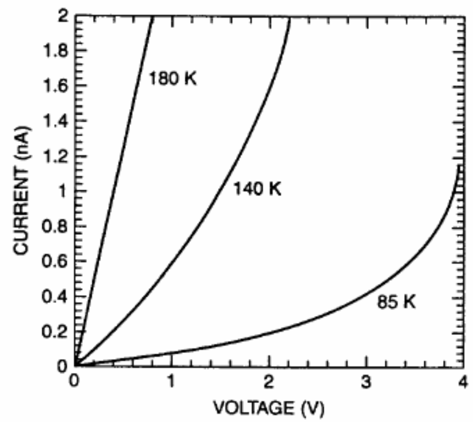

Figure 6.14. Measured current–voltage relationship for a two-dimensional linked cluster array at the temperatures of 85, 140, and 180 K. [Adapted from D. James et al., *Superlatt. Microstruct.* **18**, 275 (1995).]

Abeles, B., Sheng, Ping, Coutts, M. D. and Arie, Y. (1975) 'Structural and electrical properties of granular metal films', Advances in Physics, **24**:3, 407 - 461

Structural and electrical properties of granular metal films

By B. Abeles, Ping Sheng, M. D. Coutts and Y. Arie
RCA Laboratories, Princeton, New Jersey 08540, U.S.A.

[Received 20 January 1975]

Abstract

Granular metal films (50–200,000 Å thick) were prepared by co-sputtering metals (Ni, Pt, Au) and insulators (SiO_2, Al_2O_3), where the volume fraction of metal, x, was varied from $x=1$ to $x=0{\cdot}05$. The materials were characterized by electron micrography, electron and X-ray diffraction, and measurements of composition, density and electrical resistivity at electric fields $\mathscr{E}$ up to 10^6 V/cm and temperatures T in the range of 1·3 to 291 K. In the metallic regime (isolated insulator particles in a metal continuum) and in the transition regime (metal and insulator labyrinth structure) the conduction is due to percolation with a percolation threshold at $x \simeq 0{\cdot}5$. Tunnelling measurements on superconductor–insulator–granular metal junctions reveals that the transition from the metallic regime to the dielectric regime (10–50 Å size isolated metal particles in an insulator continuum) is associated with the breaking up of a metal continuum into isolated metal particles. In the dielectric regime the temperature dependence of the low-field resistivity is given by $\rho_L = \rho_0 \exp[2\sqrt{(C/kT)}]$, and the field dependence of the high-field, low-temperature resistivity is given by $\rho_H = \rho_\infty \exp(\mathscr{E}_0/\mathscr{E})$, where ρ_0, ρ_∞, C, and $\mathscr{E}_0$ are material constants. A simple theory based on the assumption that the ratio s/d (d-metal particle size and s-separation between particles) is a function only of composition yields expressions for $\rho(\mathscr{E}, T)$ in excellent agreement with experiment. Furthermore, the theory predicts the experimental finding that the resistivity can be expressed in terms of a universal function of the reduced variables kT/C and $\mathscr{E}/\mathscr{E}_0$. The inter-relationship between all the important physical properties of granular metals and their structure is also discussed.

- Tunneling process

Temp = 0

$$N_1(E-\mathrm{eV})f(E-\mathrm{eV})[N_2(E)(1-f(E))]$$

left occupied   right empty

f *Fermi-Dirac distribution*

I = I (→) - I (←) =

$$K\int N_1(E-\mathrm{eV})N_2(E)[f(E-\mathrm{eV})-f(E)]dE$$

$$= KN_1(E_f)N_2(E_f)\mathrm{eV} \quad = G_{nn}V$$

assume constant N, low T, small V, ohmic behavior

$$G_{nn} = KN_1(E_f)N_2(E_f)e$$

conductance

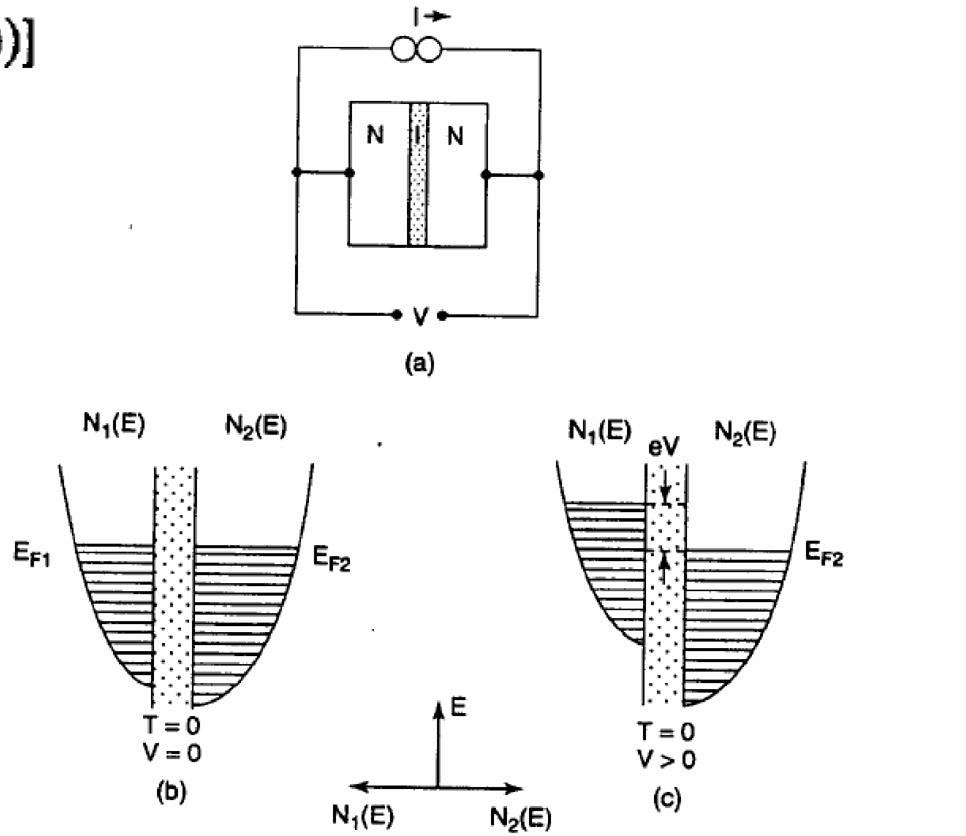

Figure 6.16. (a) Metal–insulator–metal junction; (b) density of states of occupied levels and Fermi level before a voltage is applied to the junction; (c) density of states and Fermi level after application of a voltage. Panels (b) and (c) plot the energy vertically and the density of states horizontally, as indicated at the bottom of the figure. Levels above the Fermi level that are not occupied by electrons are not shown.

- Other properties

- Enhanced resistance to oxidtion of $Fe_{73}B_{13}Si_9$
  - inherent reactivity depends on numbers of atoms
  - 30 nm Fe(Si) + Fe_2B large interface boundaries
  - FeSi segregates to interface boundaries, diffuses to surface, forms SiO_2
- 4 nm In melting temperature drops to 110 K
- Ic of superconductor increases in Nb_3Sn as grain size decreases

• Optical absorption

- In metallic nanoparticles, the peak wavelength of optical absorption depends on size and material. It is possible to fabricate high-strength transparent metal.

At high frequency, electrons behave like plasma.
For small spherical metal particle embedded in nonabsorbing medium, cluster < λ, well dispersed (non-interacting), absorption coefficient

$$\alpha = \frac{18\pi N_s V n_0 \varepsilon_2^3/\lambda}{[\varepsilon_1 + 2n_0^2]^2} + \varepsilon_2^2$$

ε1, ε2 real and imaginary dielectric const of sphere
Ns number of sphere in V
n0 refractive index of insluting glass

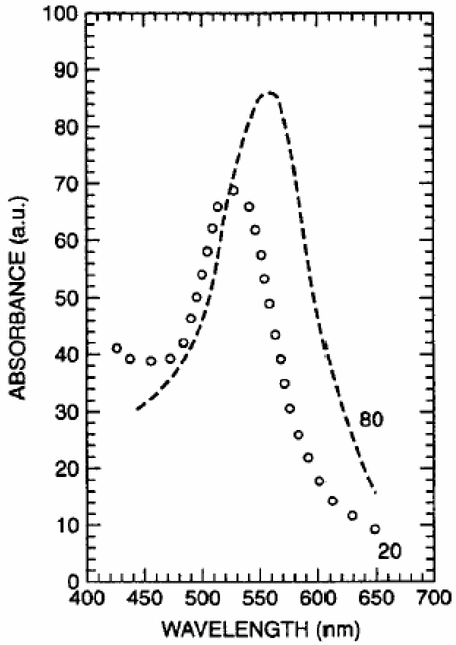

Figure 6.17. Optical absorption spectrum of 20- and 80-nm gold nanoparticles embedded in glass. (Adapted from F. Gonella et al., in *Handbook of Nanostructured Materials and Nanotechnology*, H. S. Nalwa, ed., Academic Press, San Diego, 2000, Vol. 4, Chapter 2, p. 85.)

Non-linear optical effect

Index of refraction n depends on intensity --- used as optical switchs

For n having enhanced 3rd order susceptibility,

$$n = n_0 + n_2 I$$

d < 10 nm, confinement effect alter absorption properties.

1. Melt
2. Ion implantation
   10keV ~ 10 MeV

3. Ion exchange

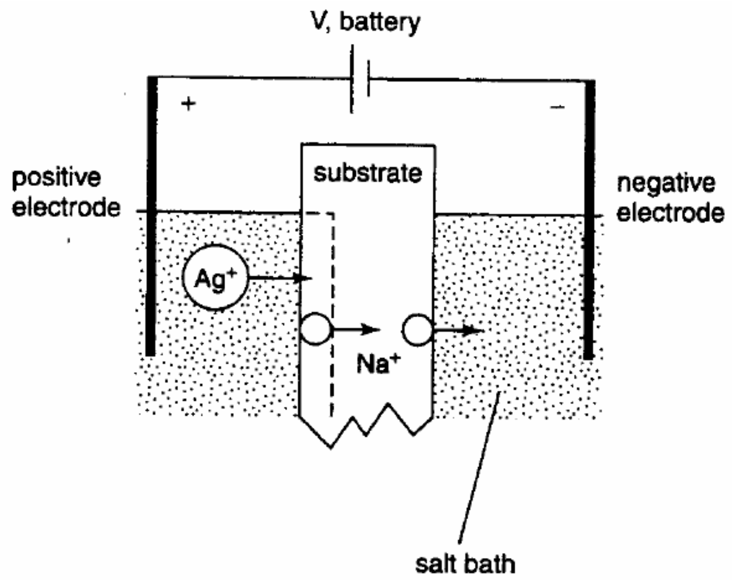

Figure 6.18. Electric field assisted ion exchange apparatus for doping glasses (substrate) with metals such as Ag^+ ions. [Adapted from G. De Marchi et al., *J. Non-Cryst. Solids* **196**, 79 (1996).]

- # Porous Si
- It is interesting because of its fluorescent property at room temp.

  Luminescence : matters absorb energy and re-emit energy as visible or near-visible light

  fluorescent : absorption and re-emission < 10^{-8} s

  phosphorescence : more delayed emission

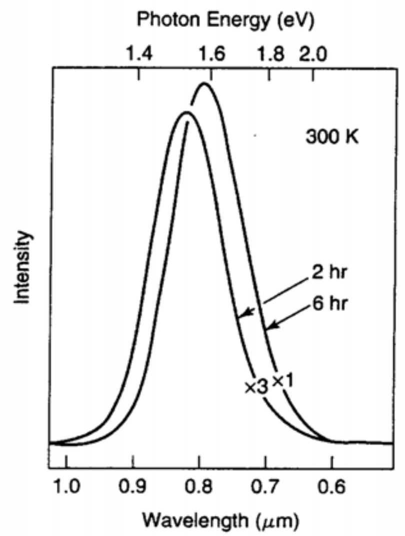

Figure 6.20. Photoluminescence spectra of porous silicon for two different etching times at room temperature. Note the change in scale for the two curves. [Adapted from L. T. Camham, *Appl. Phys. Lett.* **57**, 1046 (1990).]

Bandgap ~1.125eV at 300K
0.96 – 1.20 eV weak fluorescence

Strong photon-induced luminescence above 1.4 eV

the reason could be
oxides on the surface of pores
surface defect states
quantum wires, dots, and confinement
surface state on quantum dots

- Anisotropic etching
    - Porous silicon
    - Fabrication of AFM tips
    - Anodized aluminum oxide (AAO)

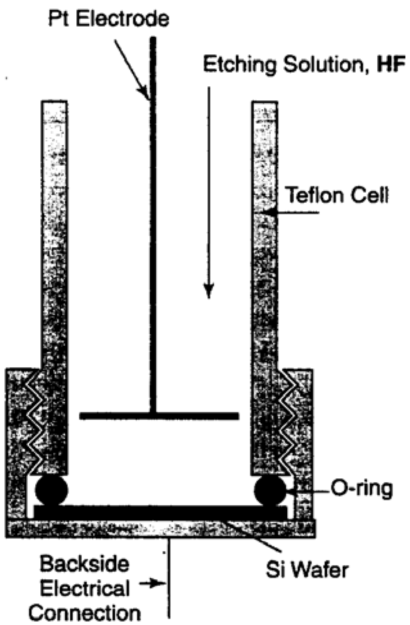

Figure 6.21. A cell for etching a silicon wafer in a hydrogen fluoride (HF) solution in order to introduce pores. (With permission from D. F. Thomas et al., in *Handbook of Nanostructured Materials and Nanotechnology*, H. S. Nalwa, ed., Academic Press, San Diego, 2000, Vol. 4, Chapter 3, p. 173.)

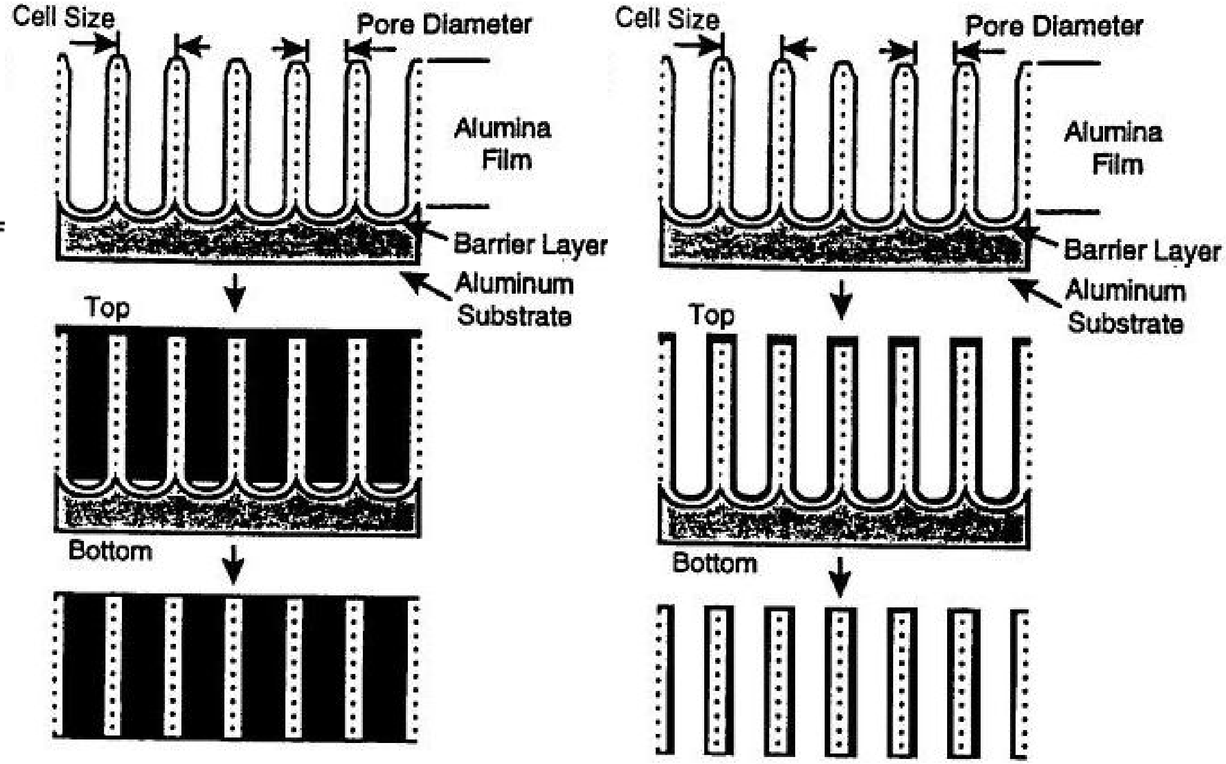

AAO template with Pb nanowires

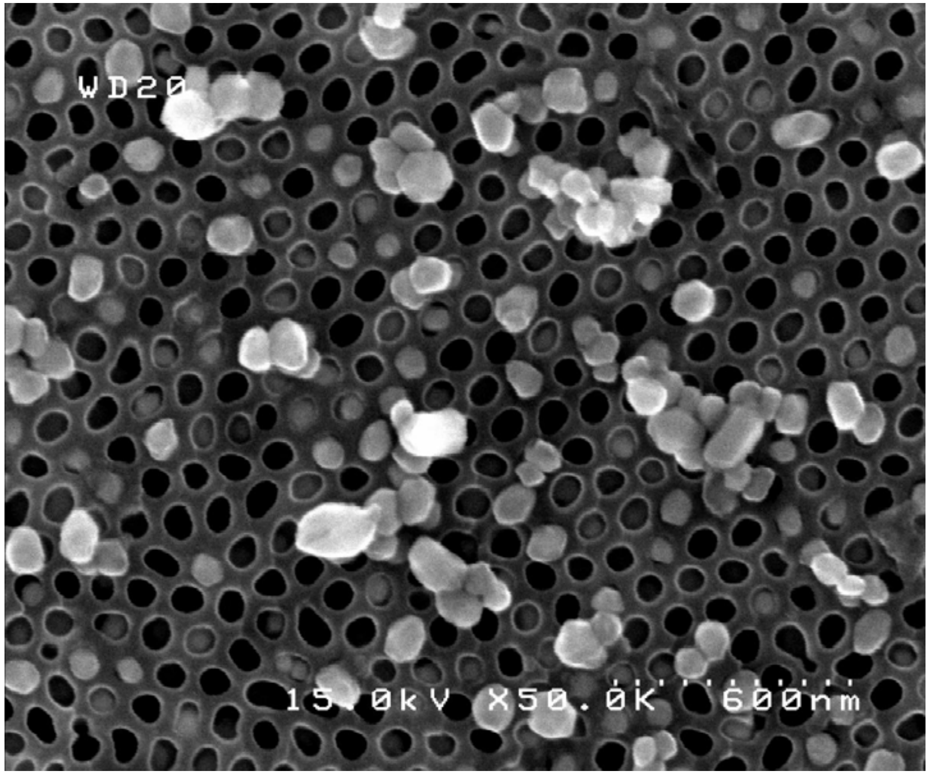

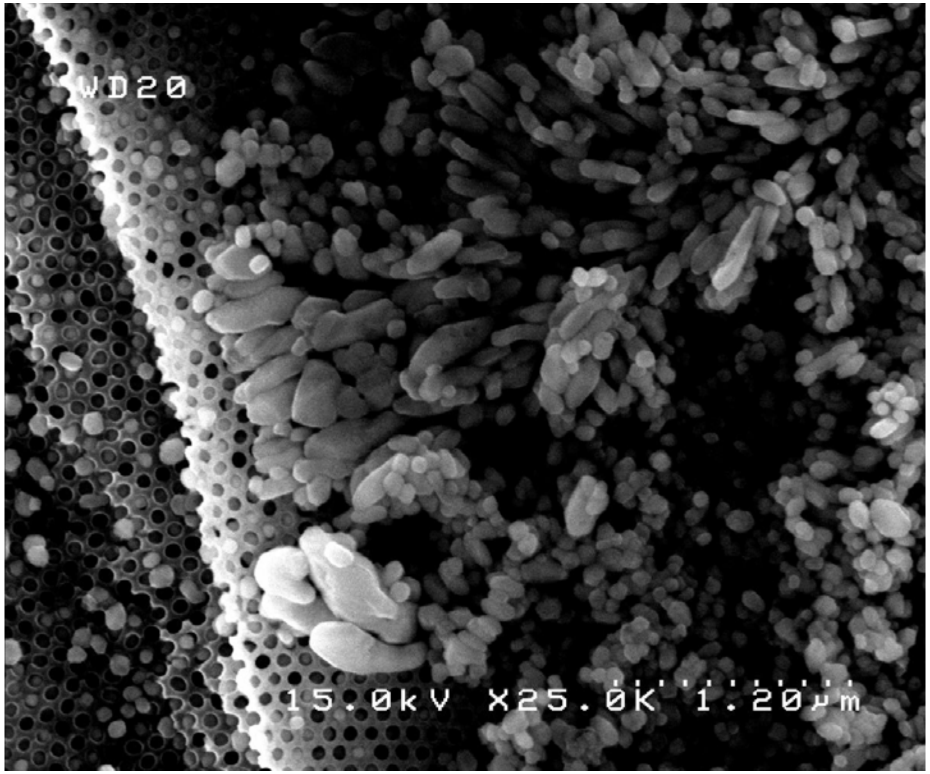

TEM image of Ni/Pb multilayer nanowire

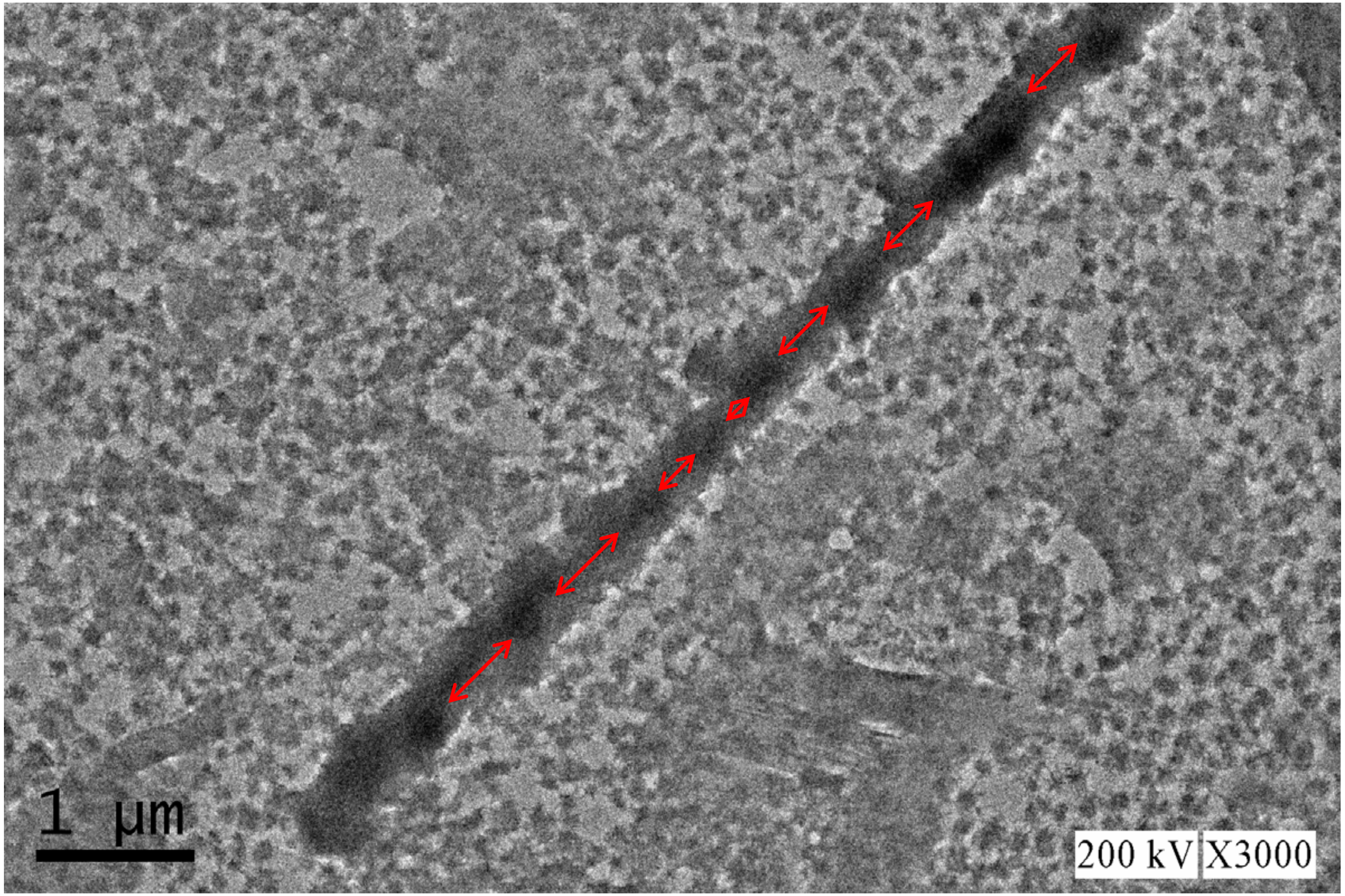

Ni : 450 ± 150 nm Pb : 340 ± 30 nm

Fabrication of AFM tips

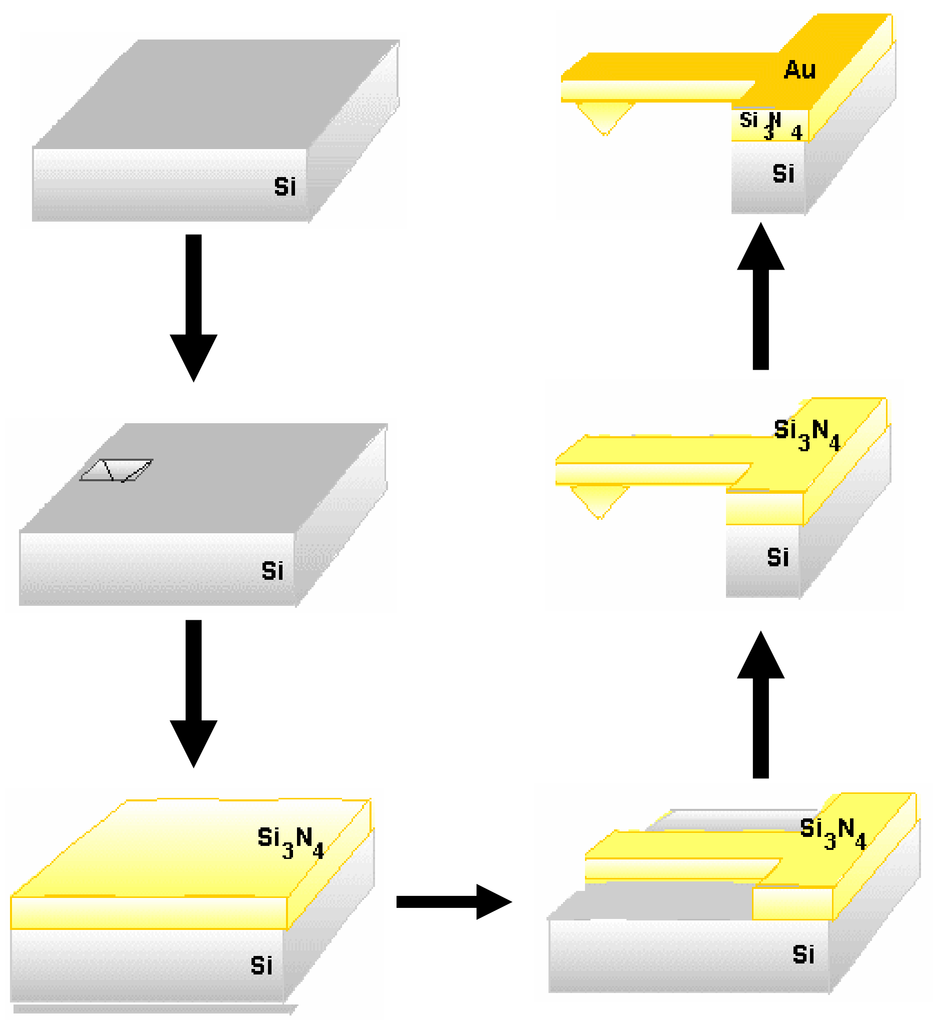

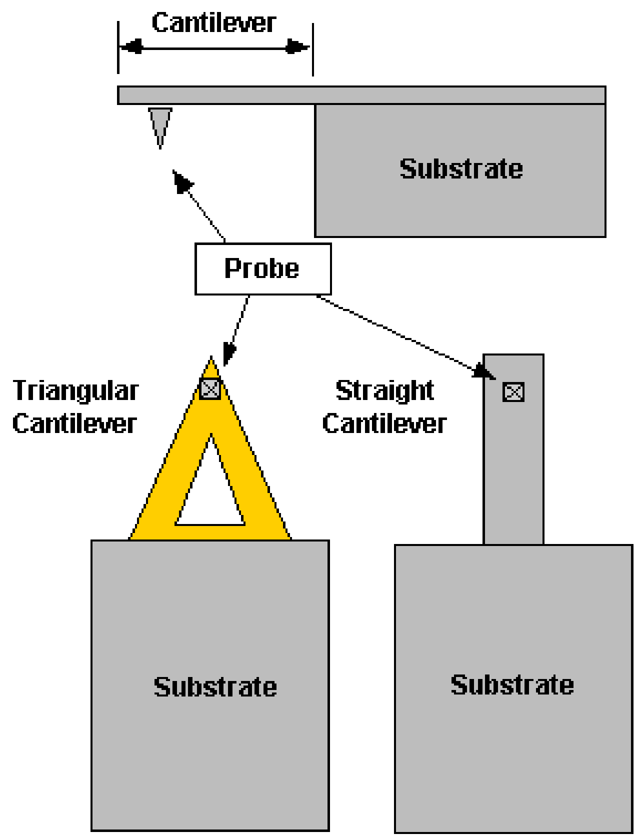

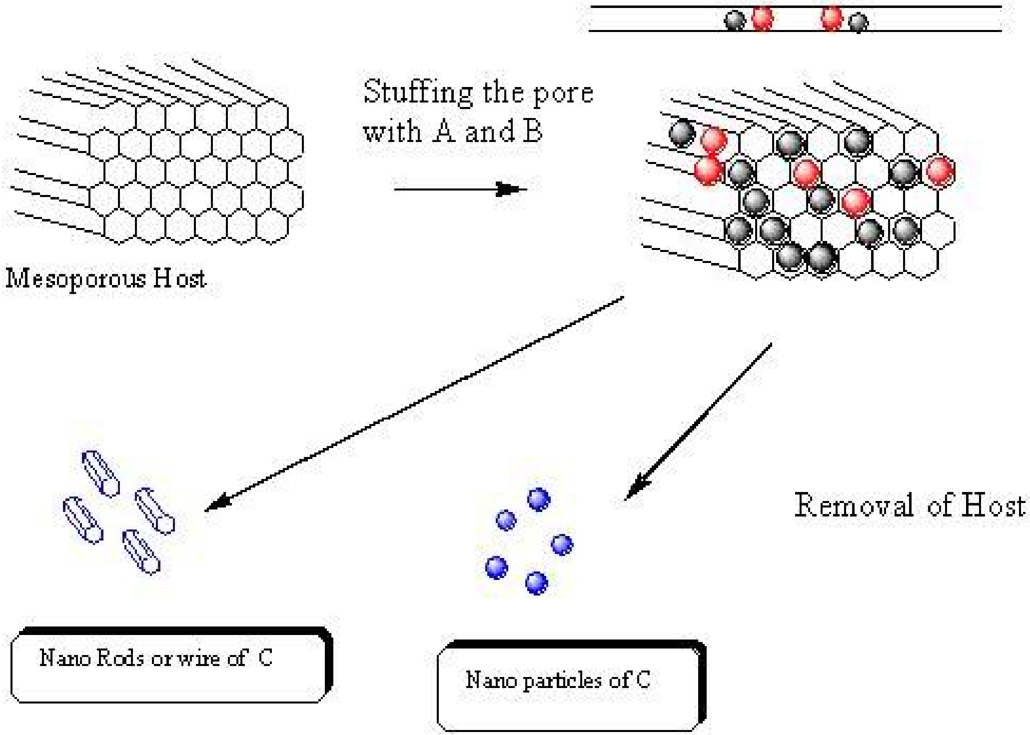
Stuffing the pore
with A and B
Mesoporous Host
Removal of Host
Nano Rods or wire of C
Nano particles of C

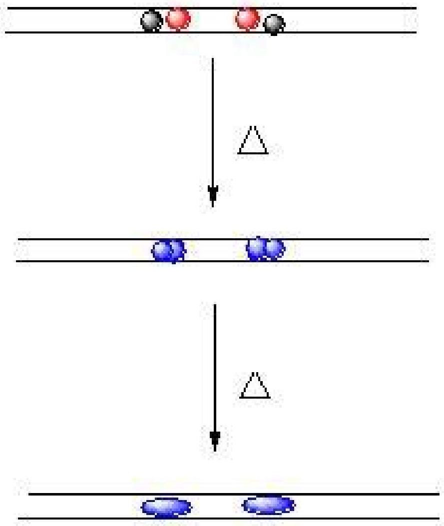
△
△

Nanostructured crystals

Natural

B_{12}, C_{60}

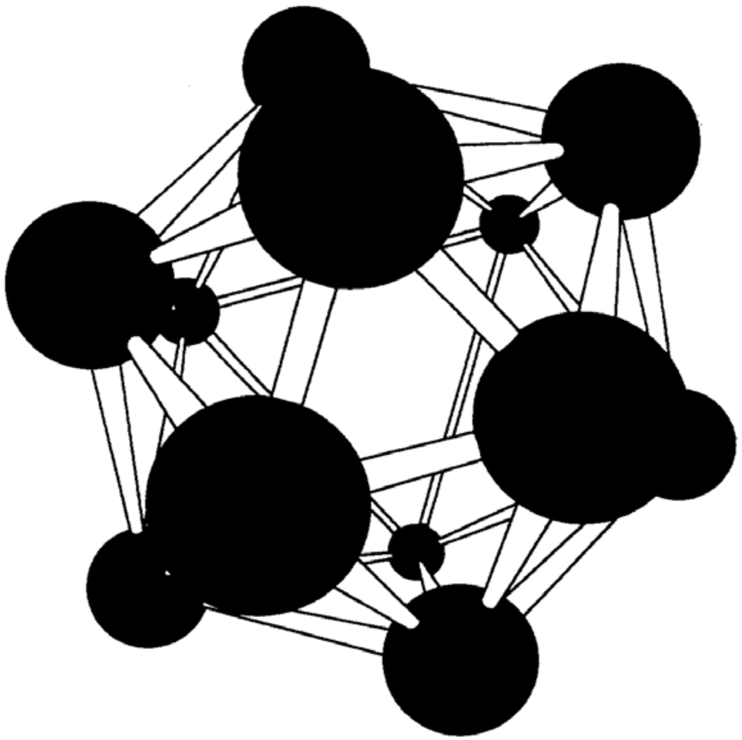

Figure 6.22. The icosohedral structure of a boron cluster containing 12 atoms. This cluster is the basic unit of a number of boron lattices.

Nanostructured crystals

Artificial

- computational predictions
- nanoparticles in Zeolites
- Au_m, Ag_m, Glass, and plastic nanospheres

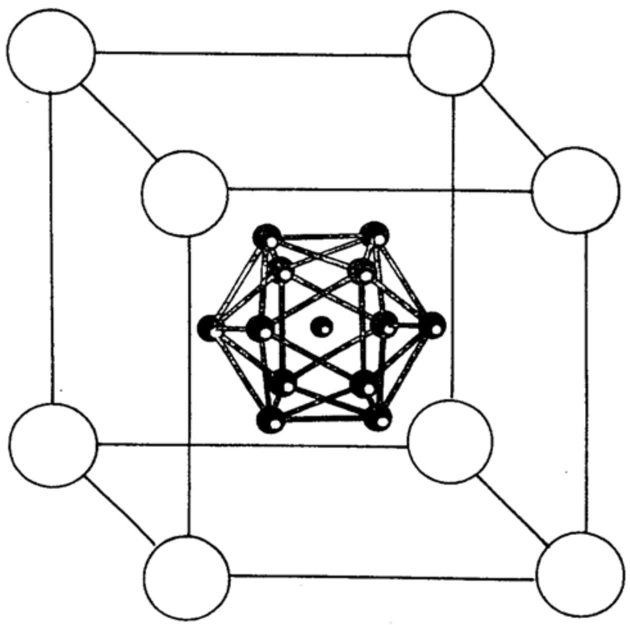

Figure 6.23. Possible body-centered structure of a lattice made of Al_{13} nanoparticles and potassium (large circles). [Adapted from S. N. Khanna and P. Jena, *Phys. Rev.* **51**, 13705 (1995).]

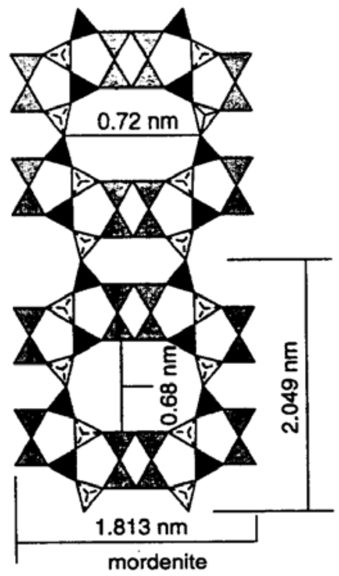

Figure 6.25. Illustration of long parallel channels in a crystal of mordenite, an orthrorhombic variety of zeolite $(Ca,Na_2,K_2)(Al_2Si_{10})O_{24} \cdot 7H_2O$. (Adapted from S. G. Romanov et al., in *Handbook of Nanostructured Materials and Nanotechnology*, H. S. Nalwa, ed., Academic Press, San Diego, 2001, Vol. 4, Chapter 4, p. 238.)

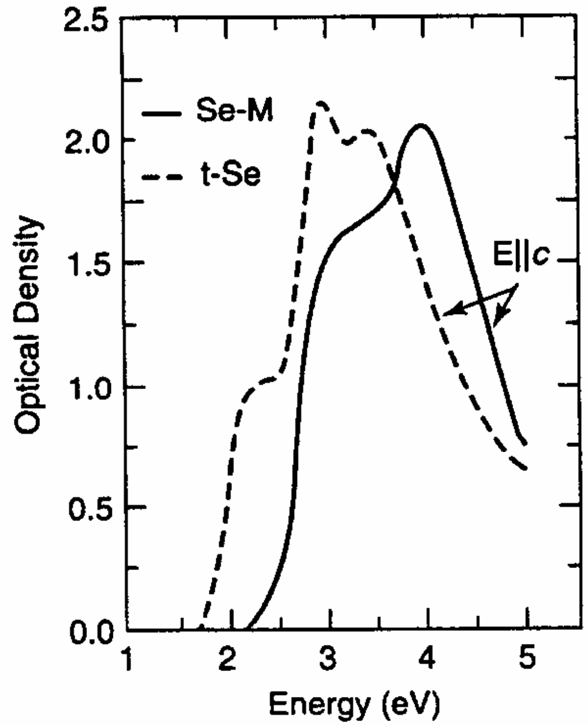

Figure 6.26. Optical absorption spectra of chains of selenium atoms in mordenite (solid line, Se–M) and in crystalline selenium (dashed line, t-Se) showing the shift in the peak of the absorption, and the change in shape. [With permission V. N. Bogomolov, *Solid State Commun.* **47**, 181, (1983).]

Nanoparticle lattice in colloidal Suspensions

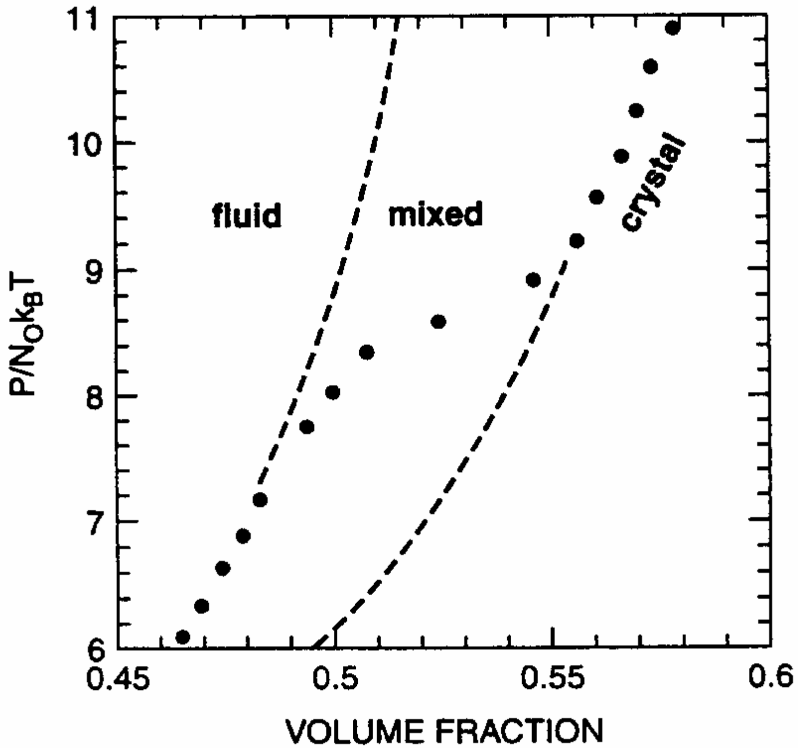

Figure 6.27. Equations of state (dashed curves) plotted as a function of fraction of 720-nm styrene spheres in a 3-mM salt solution. The constant N_0 is Avogadro's number. [Adapted from A. P. Gast and W. B. Russel, *Phys. Today* (Dec. 1998.)]

Kirkwood-Alder transition

Photonic cystal

free electrons in a metal

$$\Psi_{k[r]} = \left[\frac{1}{V}\right]^{1/3} e^{ik\cdot r}$$

$$p = \hbar k$$
$$k = 2\pi / \lambda$$
$$E = h^2 k^2 / 8\pi^2 m$$

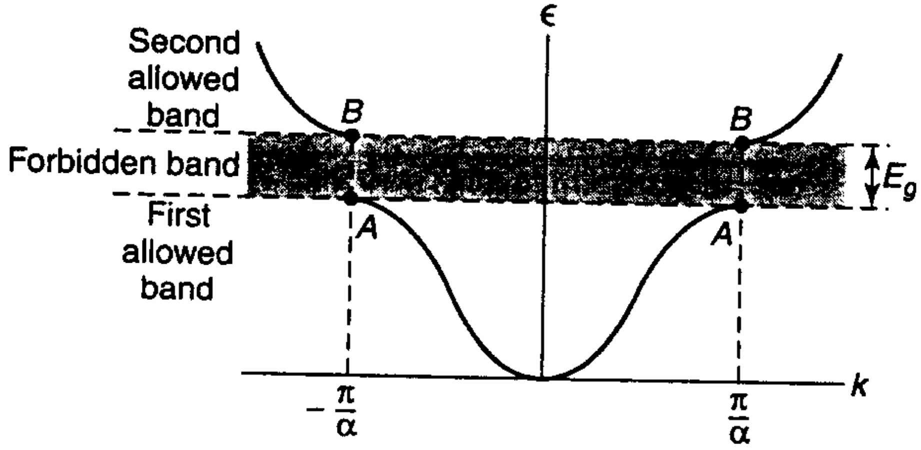

Figure 6.29. Curve of energy *E* plotted versus wavevector *k* for a one-dimensional line of atoms.

$$\nabla^2 H(r) + \varepsilon\left[\frac{\omega^2}{c^2}\right]H(r) = 0$$

H magnetic field of EM radiation

ε Dielectric constant (8.9 for Al_2O_3)

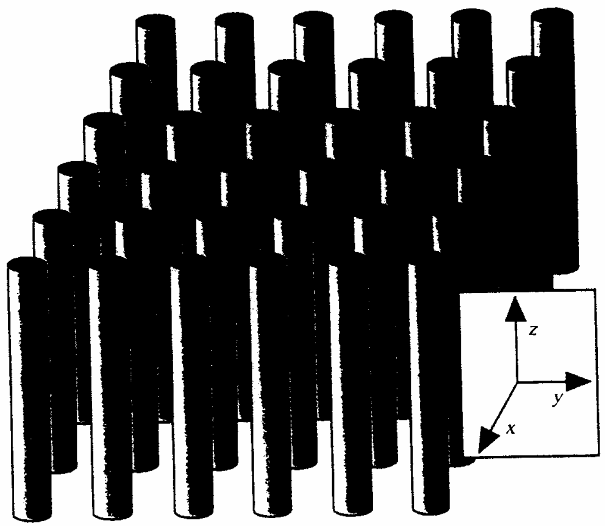

Figure 6.30. A two-dimensional photonic crystal made by arranging long cylinders of dielectric materials in a square lattice array.

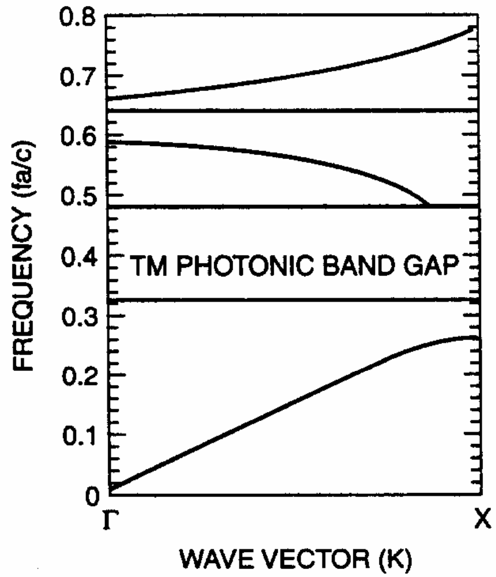

Air band

Dielectric band

Figure 6.31. A part of the dispersion relationship of a photonic crystal mode, TM, of a photonic crystal made of a square lattice of alumina rods. The ordinate scale is the frequency *f* multiplied by the lattice parameter *a* divided by the speed of light *c*. [Adapted from J. D. Joannopoulos, *Nature* **386**, 143 (1997).]

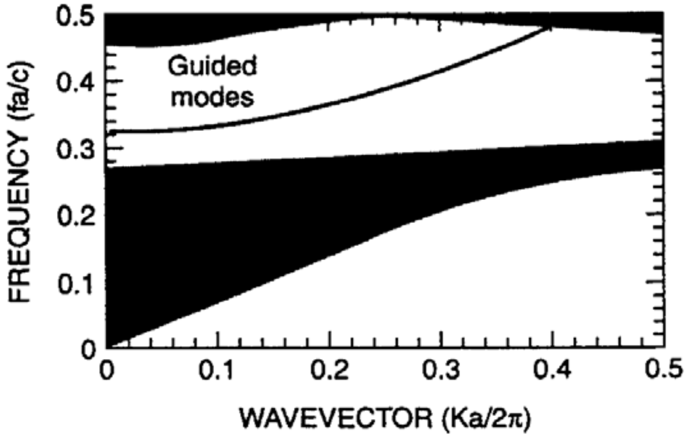

Figure 6.32. Effect of removing one row of rods from a square lattice of a photonic crystal, which introduces a level (guided mode) in the forbidden gap. The ordinate scale is the frequency f multiplied by the lattice parameter a divided by the speed of light c. [Adapted from J. D. Joannopoulos, *Nature* **386**, 143 (1997).]

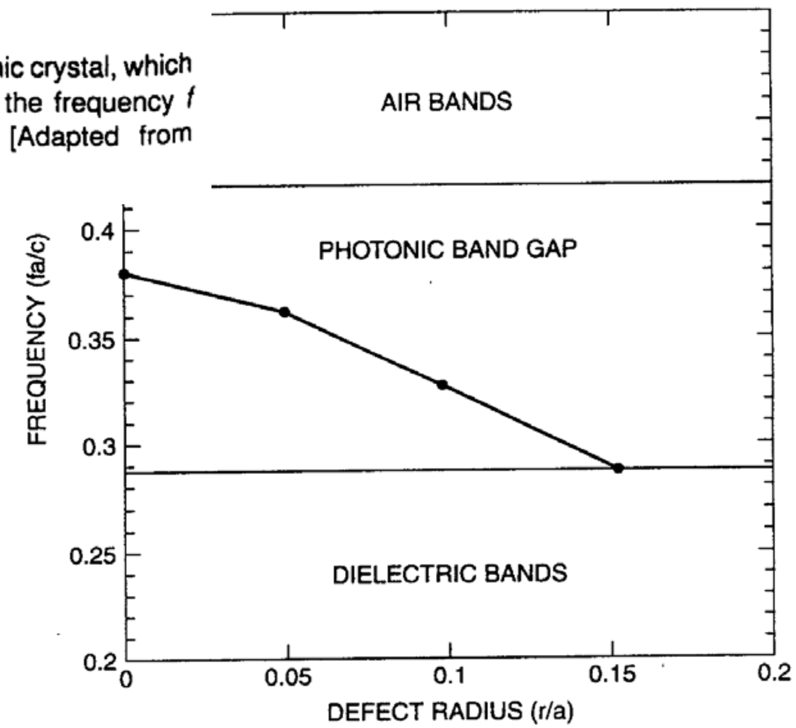

Figure 6.33. Dependence of frequency of localized states in the band gap formed on the radius r of a single rod in the square lattice. The ordinate scale is the frequency f multiplied by the lattice parameter a divided by the speed of light c. [Adapted from J. D. Joannopoulos, *Nature* **386**, 143 (1997).]

APPLIED PHYSICS LETTERS **88**, 101109 2006

Fabricating subwavelength array structures using a near-field photolithographic method

Wei-Lun Chang, Yu-Jen Chang, and Pei-Kuen Weia

Research Center for Applied Sciences, Academia Sinica, Taipei 11529, Taiwan, Republic of China

Pei Hsi Tsao

Department of Physics, National Taiwan University, Taipei 10654, Taiwan, Republic of China

This work presents a photolithographic approach for producing high aspect ratio arrays in photoresist. The photomask is composed of hexagonal/square rod arrays with a thickness of 0.2 m and a period of 600 nm. Illuminating the photomask with a blue laser generates periodically focused beams up to 1 m long and less than 300 nm wide. A hexagonal rod array provides a better focused beam than a square array due to its higher symmetry. Finite-difference time-domain calculations elucidate the existence of long focused beams above the photomask. Optical near-field measurements verified those subwavelength beams originating from the rod regions. DOI: 10.1063/1.2185249

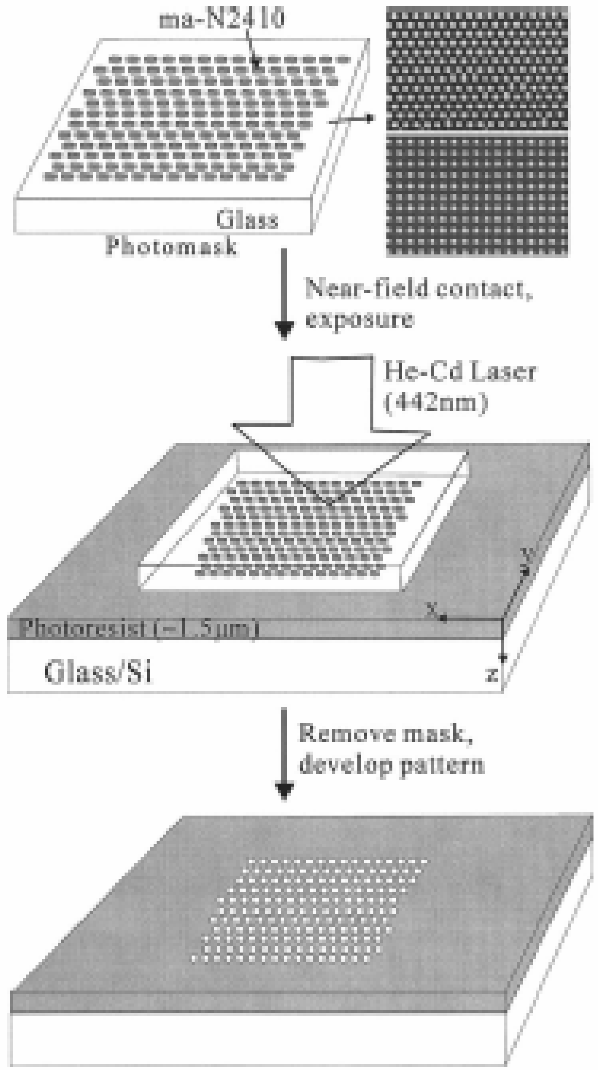

FIG. 1. The experimental setup for the photolithographic process. A transparent photomask comprised of a 2 mm thick glass substrate and a 0.2 μm thick air-rod array. Hexagonal and square arrays were made by using electron beam lithography. Both have the same rod diameter (300 nm) and period (60 nm).